Research Article

Xinxin Lian, Yuanjiang Lv, Haoliang Sun*, David Hui, and Guangxin Wang*

Effects of Ag contents on the microstructure and SERS performance of self-grown Ag nanoparticles/Mo–Ag alloy films

https://doi.org/10.1515/ntrev-2020-0058
received July 12, 2020; accepted August 02, 2020

Abstract: Ag nanoparticles/Mo–Ag alloy films with different Ag contents were prepared on polyimide by magnetron sputtering. The effects of Ag contents on the microstructure of self-grown Ag nanoparticles/Mo–Ag alloy films were investigated using XRD, FESEM, EDS and TEM. The Ag content plays an important role in the size and number of uniformly distributed Ag nanoparticles spontaneously formed on the Mo–Ag alloy film surface, and the morphology of the self-grown Ag nanoparticles has changed significantly. Additionally, it is worth noting that the Ag nanoparticles/Mo–Ag alloy films covered by a thin Ag film exhibits highly sensitive surface-enhanced Raman scattering (SERS) performance. The electric field distributions were calculated using finite-difference time-domain analysis to further prove that the SERS enhancement of the films is mainly determined by "hot spots" in the interparticle gap between Ag nanoparticles. The detection limit of the Ag film/Ag nanoparticles/Mo–Ag alloy film for Rhodamine 6G probe molecules was 5×10^{-14} mol/L. Therefore, the novel type of the Ag film/Ag nanoparticles/Mo–Ag alloy film can be used as an ideal SERS-active substrate for low-cost and large-scale production.

Keywords: Ag nanoparticles, Ag content, SERS-active substrate

1 Introduction

Surface-enhanced Raman scattering (SERS) technique, a highly sensitive fingerprint identification tool [1], has shown enormous application potential in various fields such as biomedical science [2], environmental monitoring [3], food and drug safety [4–6], catalysis [7], etc. Due to the localized surface plasmonic resonance effect, SERS provides a large Raman signal enhancement for molecules close to the plasma nanostructures [8,9]. SERS technology has been proved as a promising method for the rapid and sensitive detection of chemicals and biochemicals [10–12]. At the same time, it is crucial to prepare high-performance SERS substrates in order to achieve an efficient SERS detection.

The size, morphology and the composition of various kinds of nanoparticles can be controlled by physical and chemical methods in order to prepare SERS substrates with excellent properties [13–15]. Metal colloids are the first type of commonly used SERS substrates, mainly because of its effortless preparation and large SERS signals enhancement [16]. However, avoiding the spontaneous aggregation of colloidal metal nanoparticles is still a challenging problem. Nowadays, this challenge can be solved using some novel techniques, including inkjet printing [17], oblique angle deposition [18], lithography [19], vacuum thermal evaporation [20] and self-assembly techniques [21]. Researchers generally use these technologies to uniformly distribute metal nanoparticles on specific support substrates. In comparison with the brittle silicon and glass SERS substrates, it is worth noting that the flexible SERS substrates are easy to cut and suitable for test objects with complex shape surface [22]. Therefore, it is urgent to develop a sensitive, uniform and low-cost flexible SERS substrate, which can

* **Corresponding author: Haoliang Sun,** School of Materials Science and Engineering, Henan University of Science and Technology, Luoyang, 471003, China; Collaborative Innovation Center of Nonferrous Metals Henan Province, Luoyang, 471003, China, e-mail: sunhlwm@163.com
* **Corresponding author: Guangxin Wang,** School of Materials Science and Engineering, Henan University of Science and Technology, Luoyang, 471003, China, e-mail: wgx58@126.com
Xinxin Lian, Yuanjiang Lv: School of Materials Science and Engineering, Henan University of Science and Technology, Luoyang, 471003, China
David Hui: University of New Orleans, Department of Mechanical Engineering, New Orleans, LA70148, United States of America

promote the practical application of SERS substrate. The commercial tape with colloidal gold nanoparticles can be used as a novel flexible and adhesive SERS substrate to effectively extract objects from complex surfaces [23], which is expected to bring the SERS technology closer to real applications. The Au@Ag/PMM/qPCR-PET film chip was applied as a stable and high-performance SERS chip for highly sensitive sensing of thiabendazole residues in fruit juices [24]. The flexible SERS substrates can be integrated into portable Raman spectroscopes for point-of-care diagnostics [25], which are conceivable to penetrate global markets and have important economic value and social significance.

A uniform, stable, highly ordered and controllable nanoparticle film can be prepared by self-assembly method [26], which can improve the reproducibility and sensitivity of SERS detection. A previous study reported that the annealed Ag–Zr film deposited on polyimide (PI) can produce a new type of particle/film structure [27], which is significantly different from the traditional granular film [28–31]. Considering that the Ag nanoparticles spontaneously formed on the surface of the annealed Ag–Zr alloy films and the nanophase effects in copper alloys [27,32–37], we attempt to self-grown Ag nanoparticles with different morphologies on the surface of the deposited Mo–Ag alloy films by adjusting the Ag content at room temperature. If this purpose can be achieved, a new type of SERS substrate with excellent performance can be obtained by combining the Ag nanoparticles with high SERS sensitivity and the Mo–Ag alloy films with good repeatability at room temperature. The SERS enhancement was characterized using Rhodamine 6G (R6G) probe molecule on the Ag nanoparticle/Mo–Ag alloy film. The effects of Ag contents on the microstructure and SERS performance of the Ag nanoparticles/Mo–Ag alloy film were investigated.

2 Experiment

2.1 Fabrication of the Ag nanoparticles/Mo–Ag alloy film

Mo–Ag alloy films with different Ag contents were deposited on flexible PI using JCP-350M2 high-vacuum multitarget magnetron sputtering. The sputtering target composed of a 99.99 at% molybdenum (Mo) target (Ø 50 mm × 4 mm) overlaid with several 99.99 at% silver (Ag) plates (5 mm × 5 mm × 1 mm). The Ag contents in the Ag nanoparticles/Mo–Ag alloy films were determined by the number of Ag plates placed on Mo target.

The PI substrate was cleaned with acetone, deionized water and alcohol for 10 min, respectively, and the

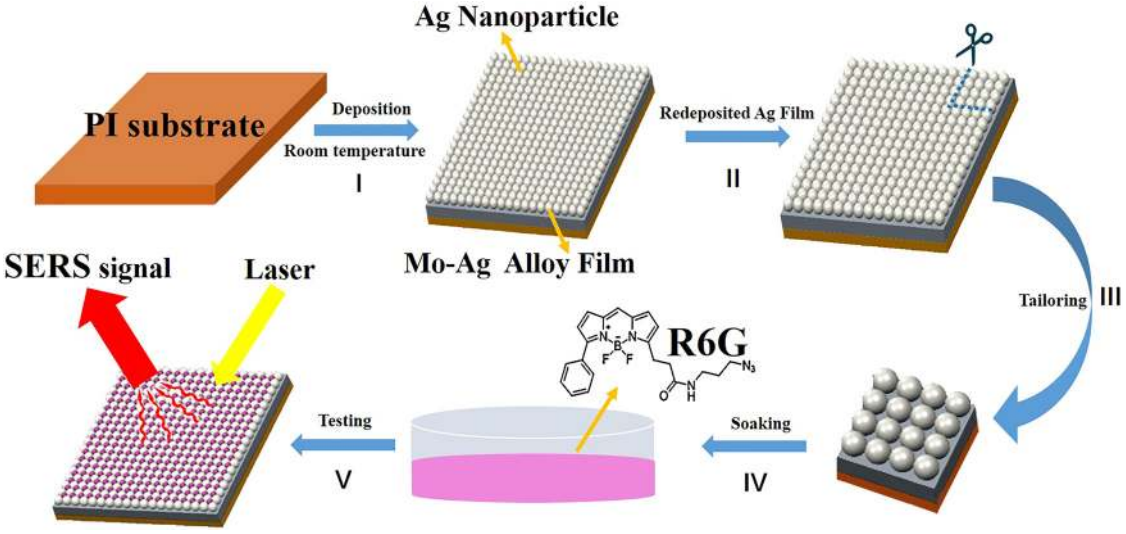

Figure 1: Schematic diagram of the Ag film/Ag nanoparticles/Mo–Ag alloy film formation and detection process of SERS performance: (I) the Mo–Ag alloy films were deposited on the flexible PI substrate at room temperature. (II) A layer of Ag film was further sputtered on the surface of the Ag nanoparticles/Mo–Ag alloy films. (III) The Ag film/Ag nanoparticles/Mo–Ag alloy film was tailored into 5 × 5 mm pieces. (IV) The Ag film/Ag nanoparticles/Mo–Ag alloy films were soaked in R6G solutions. (V) Using Raman spectrometer to test the SERS performance of the Ag film/Ag nanoparticles/Mo–Ag alloy films.

PI substrate was fixed on the substrate holder after drying. In order to reduce the influence of impurity gas in the chamber, the vacuum degree of the chamber is pumped to 5×10^{-4} Pa. The argon flow rate, sputtering power and sputtering pressure were adjusted to 40 sccm, 100 W and 0.4 Pa, respectively. The impurities on the target surface were removed by presputtering for 5 min and then sputtered for 10 min to prepare Mo–Ag alloy films. Unless otherwise mentioned, all experiments were carried out at room temperature.

2.2 Characterization of the Ag nanoparticles/Mo–Ag alloy film

X-ray diffractometer (Bruker-AXS D8 Advance) and transmission electron microscopy (TEM, JEM-2100) were used to characterize the phase structure and the crystal structure of the Ag nanoparticles/Mo–Ag alloy films. X-ray diffractometer uses a Cu target (λ = 0.1541 nm), and the voltage and current parameters are set at 40 kV and 40 mA, respectively. The scanning speed is 6°/min, the step size is 0.02° and the range of angle is 20°–90°. The high voltage of the TEM is 200 kV. The surface morphology and the composition of the Ag nanoparticles/Mo–Ag alloy films were observed and confirmed using a field emission scanning electron microscope (FESEM, JSM-7800F) with energy dispersive spectroscopy (EDS). The electric field distributions were calculated using finite-difference time-domain (FDTD) analysis. The number and average size of the nanoparticles on the surface of the Mo–Ag alloy films were measured by ImageJ software.

2.3 Preparation and measurement of SERS substrate

Figure 1 shows the schematic diagram of the Ag film/Ag nanoparticles/Mo–Ag alloy film formation and the detection process of SERS performance. The Mo–Ag alloy films were deposited on flexible PI substrate by DC magnetron sputtering (Figure 1-I). Considering that the Mo and Ag are immiscible at room temperature [38] and the initial Mo–Ag alloy film will be in a metastable state, the Mo–Ag alloy films form a stable structure through atoms diffusion along the surface and grain boundaries under the relaxation of residual stress and distortion energy [39]. As a result, a large amount of the Ag nanoparticles were self-formed on the surface of the Mo–Ag alloy film by adjusting the Ag content. Subsequently, a pure Ag target (99.99 %, Ø 50 mm × 4 mm) was used to further sputter a layer of Ag film on the surface of the Ag nanoparticles/Mo–Ag alloy films under the same sputtering parameters as the preparation of the Mo–Ag alloy film (Figure 1-II). The most common probe molecule, R6G, was selected to measure the performance of the SERS substrate [40]. The Ag film/Ag nanoparticles/Mo–Ag alloy films were tailored into 5 × 5 mm pieces (Figure 1-III) and soaked in different concentrations of R6G in aqueous solutions (20 mL) for 60 min (Figure 1-IV). After the droplet has been evaporated naturally, samples were characterized using the laser wavelength 532 nm Raman spectrometer (Invia, Renishaw, UK) with 50× objective lens (N.A. = 0.80) (Figure 1-V). The laser excitation energy and spot, respectively, were 5 mW and 2 μm, respectively. The diffraction grid was 1,200 g/mm. The Raman spectra were collected in the range of 200–2,000 cm^{-1} with the acquisition time of 1 s.

3 Results and discussions

3.1 Surface morphology of the Ag nanoparticles/Mo–Ag alloy films

Figure 2 shows the surface morphology of the pure Ag film, the pure Mo film and the Mo–Ag alloy films with different Ag contents. The surfaces of the Ag film and the Mo film are smooth without defects and cracks, as shown in Figure 2(a) and (b). However, a large amount of nanoparticles with different shapes are spontaneously formed on the surface of the Mo–Ag alloy films, as shown in Figure 2(c–f). This is different from the surface morphology of pure Ag film and pure Mo film. According to the EDS spectra in Figure 2(c1–f1), the Ag contents of the Mo–Ag alloy films in Figure 2(c–f) are 18.0, 25.5, 38.5 and 51.2 at%, respectively. The cross-sectional morphology of the Mo–Ag alloy films is shown in Figure 2(c2–f2), and the relative position relationship between the self-formed particles and the film is obviously different from the particles embedded in the traditional film [26]. As shown in Figure 2(c), some fine nanoparticles self-grow on the surface of the Mo-18.0 at% Ag film. Comparing with the Mo-18.0 at% Ag film, the number of nanoparticles on the surface of the Mo-25.5 at% Ag films has increased and distributed evenly as shown in Figure 2(d). More importantly, the morphology of the nanoparticle on the surface of the Mo-25.5 at% Ag film is

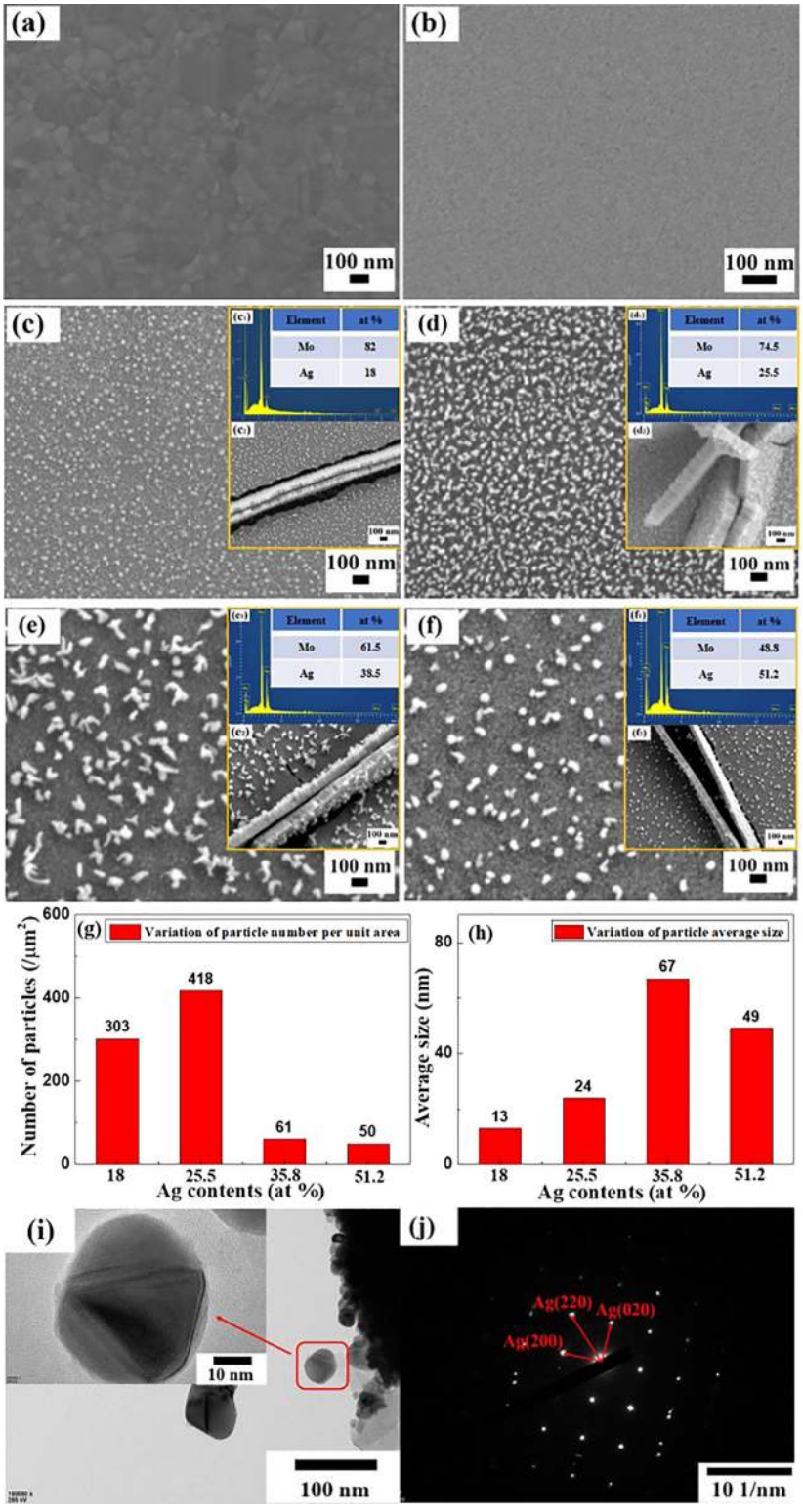

Figure 2: (a) Surface morphology of the Ag film. (b) Surface morphology of the Mo film. (c) SEM image, (c_1) EDS spectrum and (c_2) cross-sectional morphology of the Mo-18.0 at% Ag films. (d) SEM image, (d_1) EDS spectrum and (d_2) cross-sectional morphology of the Mo-25.5 at % Ag films. (e) SEM image, (e_1) EDS spectrum and (e_2) cross-sectional morphology of the Mo-38.5 at% Ag films. (f) SEM image, (f_1) EDS spectrum and (f_2) cross-sectional morphology of the Mo-51.2 at% Ag films. (g) Variation of the nanoparticle number per unit area on the film surface with Ag content. (h) Variation of the average particle size on the film surface with Ag content. (i) The TEM pattern of the nanoparticles/Mo–Ag alloy film and nanoparticle magnification. (j) The SAED pattern of the nanoparticle in (i).

irregular "worm-like," which is different from the regular nanoparticles obtained on the surface of the annealed Ag–Zr alloy films [27]. The average nanoparticle size on the surface of the Mo-38.5 at% Ag film is increased by 43 nm compared with the nanoparticle size on the surface of the Mo-25.5 at% Ag film. However, the number of the nanoparticles on the Mo-38.5 at% Ag film is significantly lower than on the 25.5 at% film. Moreover, it is worth noting that some nanoparticles on the surface of the Mo-38.5 at% Ag film have changed from irregular "worm-like" to polyhedron as shown in Figure 2(e). This is significantly different from the morphological transformation from flower-shaped particles to polyhedral particles on the surface of the annealed Mo–Cu alloy film observed previously [41]. The driving force for the formation of the Ag nanoparticles decreases with the increase of Ag content, resulting in a decrease in the number and particle size of the Ag nanoparticles in the Mo-51.2 at% Ag film compared with the Mo-38.5 at% Ag film. Furthermore, the morphology of the nanoparticles on the surface of the Mo-51.2 at% Ag film has completely been changed into polyhedron as shown in Figure 2(f). The number and average size of the nanoparticles on the surface of the Mo–Ag alloy films were measured by ImageJ software, as shown in Figure 2(g) and (h). The nanoparticles were taken from the surface of the Mo-51.2 at% Ag films and proved to be single-crystal Ag nanoparticle by TEM characterization as shown in Figure 2(i) and (j), respectively. Based on the above analysis, the Ag atoms on and near the film surface can easily diffuse along the grain boundaries to the triple junctions and the vacancies to aggregate and nucleate continuously with the increase of the Ag content in the Mo–Ag alloy films. Meanwhile, the adjacent Ag nanoparticles may contact with each other and grow into one Ag nanoparticle on the surface of the Mo–Ag alloy film.

3.2 XRD patterns of the Ag nanoparticles/Mo–Ag alloy films

Figure 3 shows the XRD patterns of the as-deposited Ag nanoparticles/Mo–Ag alloy film with different Ag contents. The diffraction peaks at 40.5° and 73.6° on the XRD pattern of the Mo-18.0 at% Ag films correspond to Mo(110) and Mo(211) (JCPDS No. 42-1120). Comparison with the Mo-18.0 at% Ag films, the intensity of the Mo (110) diffraction peaks of the Mo-25.5 at% Ag films and the Mo-38.5 at% Ag films decreased gradually, indicating that Ag grains have an inhibition effect on the growth of

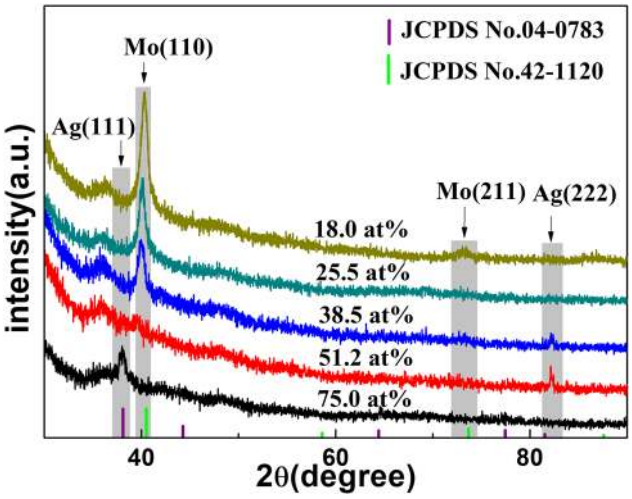

Figure 3: XRD patterns of the Ag nanoparticles/Mo–Ag alloy films with different Ag contents.

Mo grains. Furthermore, referring to Bragg formula ($2d \sin\theta = k\lambda$), the increase in the crystal surface spacing leads to the shift in the Mo(110) diffraction peak which moves toward smaller angle as the increase in Ag content in the Mo–Ag films. This can be attributed to the distortion energy caused by the residual tensile stress between the Mo and the Ag grains. The Mo(110) diffraction peaks on the XRD pattern of the Mo-51.2 at% Ag films almost disappeared, and the Ag(222) diffraction peaks' intensity has increased. This also indicated that the Ag grains have an inhibitory effect on the growth of Mo grains. Meanwhile, the XRD patterns of the Mo-75 at% Ag films have a conspicuous peak at 38.1° corresponding to the (111) plane of Ag (JCPDS No. 04-0783). The Ag grains preferentially grow along (111) plane in the Mo-75 at% Ag films due to its low surface energy. The relatively weak diffraction peaks of the Ag nanoparticles/Mo–Ag alloy films can be ascribed to the very fine Mo and Ag grains in the alloy films.

4 Ag nanoparticles/Mo–Ag alloy films as SERS substrate

The surface morphology and Raman spectra of the Ag nanoparticles/Mo–Ag alloy films are shown in Figure 4. Despite the large number of Ag nanoparticles formed on the surface of the Mo–Ag alloy films, the SERS performance of the Ag nanoparticles/Mo–Ag alloy film is still not efficient due to the small size of the Ag

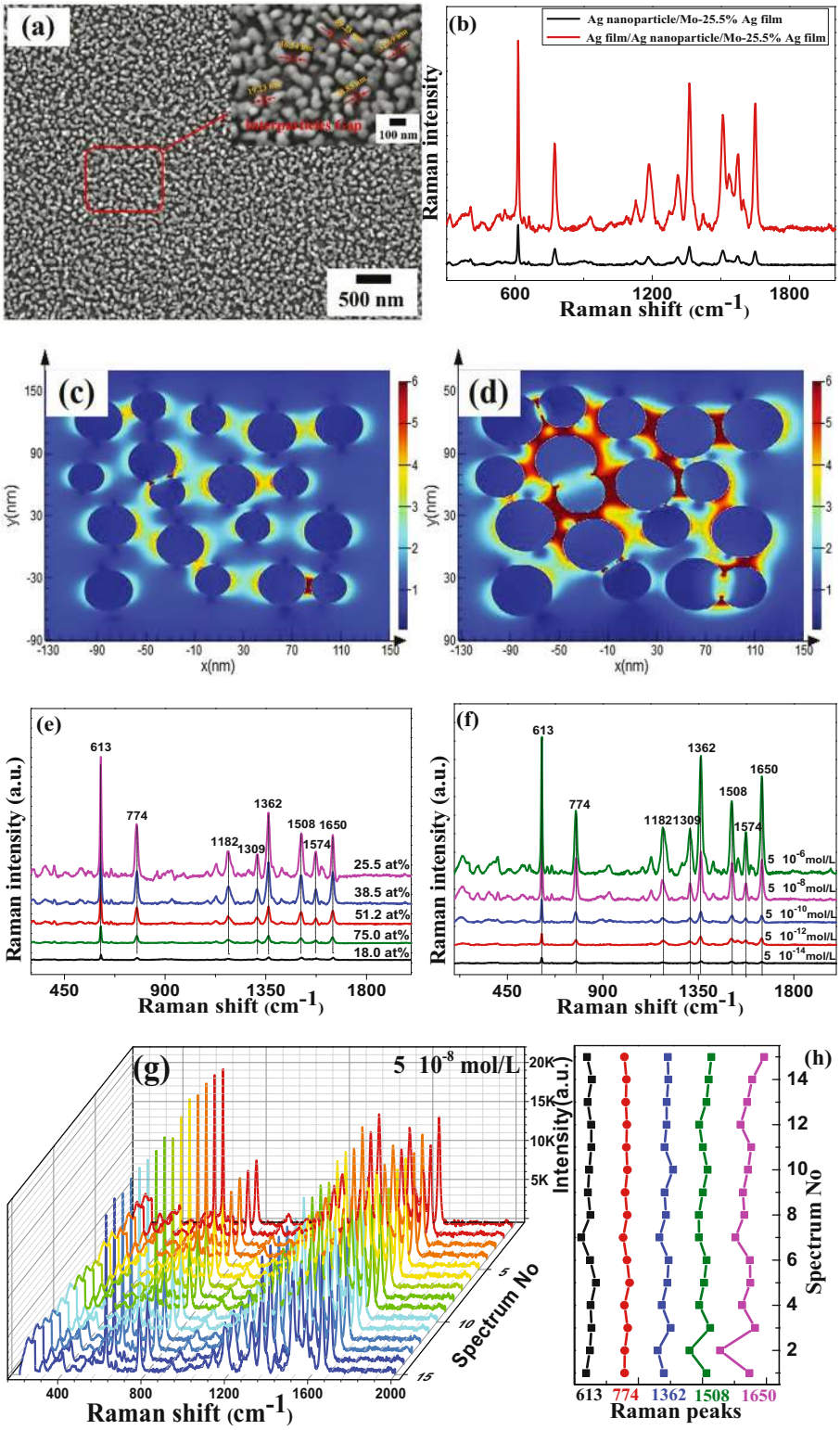

Figure 4: (a) Surface morphology of the Ag film/Ag nanoparticles/Mo-25.5 at% Ag films. (b) SERS spectra of the Ag nanoparticles/Mo-25.5 at% Ag films and Ag film/Ag nanoparticles/Mo-25.5 at% Ag films. (c) FDTD simulations of the EM field intensity of the Ag nanoparticles/Mo–Ag films and distribution of the Ag nanogaps structure. (d) FDTD simulations of the EM field intensity of the Ag film/Ag nanoparticles/Mo–Ag films and distribution of the Ag nanogaps structure. (e) SERS spectra of the Ag film/Ag nanoparticles/Mo–Ag alloy films with different Ag contents. (f) SERS spectra of the Ag film/Ag nanoparticles/Mo-25.5 at% Ag films with different concentrations of R6G solution. (g) SERS spectra of 15 randomly selected locations in the Ag film/Ag nanoparticles/Mo-25.5 at% Ag films. (h) Variation of the Raman spectra intensity at 613, 774, 1,362, 1,508 and 1,650 cm^{-1} peaks in (g), respectively.

nanoparticles [42,43]. Therefore, a 23-nm Ag film was further sputtered on the surface of the Ag nanoparticles/Mo-25.5 at% Ag film, and its surface morphology is shown in Figure 4(a). The Ag nanoparticles/Mo-25.5 at% Ag film and the Ag film/Ag nanoparticles/Mo-25.5 at% Ag film were soaked in the 5×10^{-6} mol/L R6G solution for 60 min and tested after air-dried naturally to compare the Raman intensity. As shown in Figure 4(b), the SERS performance of the Ag nanoparticles/Mo-25.5 at% Ag film after sputtering of Ag film is significantly enhanced. In order to better understand the enhancement mechanism of the Ag film/Ag nanoparticles/Mo–Ag film as an efficient SERS substrate, we have calculated the electric field distributions of the Ag nanoparticles/Mo–Ag film and the Ag film/Ag nanoparticles/Mo–Ag film using FDTD analysis, as shown in Figure 4(c) and (d). It obviously shows that smaller gaps between adjacent nanoparticles on the surface of the Ag film/Ag nanoparticles/Mo–Ag alloy film can increase the amount of "hot spots" and improve the sensitivity of the SERS substrate [44]. Thence, a thin Ag film was further sputtered on the surface of the Ag nanoparticles/Mo–Ag alloy films with different Ag contents. The intensity of the Raman peaks increases and then decreases with the increase in the Ag content as shown in Figure 4(e). This is closely related to the number, size and shape of Ag particles. Moreover, the SERS performance of the Ag film/Ag nanoparticles/Mo-25.5 at% Ag film as SERS substrate is excellent. This can be ascribed to the small gaps between adjacent nanoparticles, the irregular nanoparticle shapes and the rough surface of the films. It is worth noting that the maximum number of particles on the surface of the Mo-25.5 at% Ag alloy film leads to the best SERS performance among Mo–Ag alloy films with different Ag content. This is consistent with the largest number of Ag particles on the annealed Ag–Zr alloy film surface leading to the strongest SERS enhancement [27]. The previous studies have also indicated that the particle shape of the annealed Mo–Cu alloy film surface is crucial for the SERS enhancement [41]. The Ag film/Ag nanoparticles/Mo-25.5 at% Ag films were tailored into 5 × 5 mm pieces and soaked in the R6G solutions of 5×10^{-6}, 5×10^{-8}, 5×10^{-10}, 5×10^{-12} and 5×10^{-14} mol/L, respectively. As can be seen from Figure 4(f) that the intensity of characteristic peaks of the SERS spectra decreased with the concentration of R6G solution decreases. As the concentration of R6G solution is 5×10^{-14} mol/L, weak characteristic peaks can be observed in the Raman spectra of the Mo-25.5 at% Ag films, which is enough to identify the existence of R6G probe molecules. Therefore, the number of particles per unit area and the particle average size on the surface of the Mo-25.5 at% Ag films are 418/μm^2 and 24 nm, respectively, and it can be applied as highly effective SERS substrates for the detection of 10^{-14} mol/L R6G solution due to its abundant active "hot spots." To some extent, a large number of high-density "hot spots" are generated due to the small gap between adjacent particles, resulting in the SERS enhancement with good uniformity and reproducibility [45].

To evaluate the enhancement factor (EF) of the Ag film/Ag nanoparticles/Mo-25.5 at% Ag alloy films as SERS substrate, the average EF of the characteristic peak of 613 cm^{-1} for the R6G solution on the SERS substrates was calculated according to the following formula:

$$\mathrm{EF} = \frac{I_{\mathrm{SERS}}/N_{\mathrm{SERS}}}{I_{\mathrm{RS}}/N_{\mathrm{RS}}} = \frac{I_{\mathrm{SERS}}}{I_{\mathrm{RS}}} \times \frac{N_{\mathrm{SERS}}}{N_{\mathrm{RS}}}$$

where I_{SERS} and I_{RS} represent the peak intensity of the SERS signal and the normal Raman signal, respectively. N_{SERS} and N_{RS} are the numbers of R6G molecules in the SERS measurement and in the normal Raman measurement, respectively. Hence, the EF of the Ag film/Ag nanoparticles/Mo-25.5 at% Ag alloy films is estimated:

$$\begin{aligned}\mathrm{EF} &= \frac{1,550\ \text{(a.u.)}}{575\ \text{(a.u.)}} \\ &\quad \times \frac{5 \times 10^{-2}\ \text{mol/L} \times 50\ \text{mL} \times N_{\mathrm{A}} \times (A_{\mathrm{laser}}/A_{\mathrm{PI}}^{\mathrm{dry}})}{5 \times 10^{-14}\ \text{mol/L} \times 50\ \text{mL} \times N_{\mathrm{A}} \times (A_{\mathrm{laser}}/A_{\mathrm{SERS}}^{\mathrm{dry}})} \\ &= 2.69 \times 10^{12}\end{aligned}$$

where N_{A} is Avogadro's constant, A_{laser} is the area of laser spot, $A_{\mathrm{PI}}^{\mathrm{dry}}$ is the measurement area on the PI substrate, $A_{\mathrm{SERS}}^{\mathrm{dry}}$ is the measurement area on the SERS substrate. The measurement area on the PI substrate is the same as that on SERS substrate. The resonance Raman signal was found using 5×10^{-2} mol/L R6G solution on the blank PI substrate.

For practical applications, an efficient SERS substrate should possess not only a large number of "hot spots" to ensure high sensitivity but also the uniform distribution of "hots pots" to achieve good signal reproducibility [46,47]. Therefore, as shown in Figure 4(g), the 15 randomly selected locations on the Ag film/Ag nanoparticles/Mo-25.5 at% Ag films immersed in the 5×10^{-8} mol/L R6G solution and naturally air-dried were measured to evaluate the uniformity and reproducibility of the SERS substrate. The strongest characteristic peaks of R6G are the 613 cm^{-1} peaks (C–C–C in-plane bending), the 774 cm^{-1} peaks (C–H out-plane bending), and the

C–C stretching of 1,362, 1,508, and 1,650 cm^{-1} peaks [48]. The estimation results of the deviation of the Raman characteristic peaks of the Ag film/Ag nanoparticles/Mo-25.5 at% Ag films were shown in Figure 4(h), indicating that the films have good uniformity and reproducible SERS performance.

5 Conclusion

Mo–Ag alloy films with different Ag contents were fabricated on flexible PI substrate by DC magnetron sputtering. The addition of Ag can inhibit the growth of Mo grains in the Mo–Ag alloy films and can result in a large amount of Ag nanoparticles with different morphologies spontaneously formed on the surface of as-deposited Mo–Ag alloy films. Moreover, as the Ag content increases, the number of the Ag nanoparticles significantly increases first and then decreases, and the morphology of Ag nanoparticles has gradually evolved in the following way: spherical → "worm-like" → "worm-like" + polyhedral → polyhedral. Interestingly, the "worm-like" Ag nanoparticles/Mo-25.5 at% Ag films have abundant active "hot spots," and further sputtering of the Ag film can be used as high-efficient SERS substrates. The detection limit of the Ag film/Ag nanoparticles/Mo-25.5 at% Ag film as SERS substrate for R6G probe molecule is 10^{-14} mol/L, and the EF is 2.69×10^{12}. Therefore, the Ag film/Ag nanoparticles/Mo-25.5 at% Ag film can be used as an efficient SERS substrate for low-cost and large-scale production.

Acknowledgments: This work was financially supported by the National Natural Science Foundation of China (Grant No. U12041869), the Chinese 02 Special Fund (Grant No. 2017ZX02408003) and the Chinese 1000 Plan for High Level Foreign Experts (Grant No. WQ20154100278).

Conflict of interest: The authors declare no conflict of interest regarding the publication of this paper.

References

[1] Langer J, Aberasturi DJd, Aizpurua J, Alvarez-Puebla RA, Auguie B, Baumberg JJ, et al. Present and future of surface enhanced Raman scattering. ACS Nano. 2020;14:28–117.

[2] Jung GB, Bae YM, Lee YJ, Ryu SH, Park H-K. Nanoplasmonic Au nanodot arrays as an SERS substrate for biomedical applications. Appl Surf Sci. 2013;282:161–4.

[3] An Q, Zhang P, Li JM, Ma WF, Guo J, Hu J, et al. Silver-coated magnetite–carbon core–shell microspheres as substrate-enhanced SERS probes for detection of trace persistent organic pollutants. Nanoscale. 2012;4:5210–6.

[4] Giovannozzi AM, Rolle F, Sega M, Abete MC, Marchis D, Rossi AM. Rapid and sensitive detection of melamine in milk with gold nanoparticles by surface enhanced Raman scattering. Food Chem. 2014;159:250–6.

[5] Zhu YQ, Li MQ, Yu DY, Yang LB. A novel paper rag as 'D-SERS' substrate for detection of pesticide residues at various peels. Talanta. 2014;128:117–24.

[6] Naseer B, Srivastava G, Qadri OS, Faridi SA, Islam R, Younis K. Importance and health hazards of nanoparticles used in the food industry. Nanotechnol Rev. 2018;7(6):623–41.

[7] van Schrojenstein Lantman EM, Deckert-Gaudig T, Mank AJG, Deckert V, Weckhuysen BM. Catalytic processes monitored at the nanoscale with tip-enhanced Raman spectroscopy. Nat Nanotechnol. 2012;7(9):131.

[8] Gabudean AM, Biro D, Astilean S. Localized surface plasmon resonance (LSPR) and surface-enhanced Raman scattering (SERS) studies of 4-aminothiophenol adsorption on gold nanorods. J Mol Struct. 2011;993:420–4.

[9] Wang Z, Cai K, Lu Y, Wu HN, Li Y, Zhou QG. Insight into the working wavelength of hotspot effects generated by popular nanostructures. Nanotechnol Rev. 2019;8:24–34.

[10] Sailor MJ, Park JH. Hybrid nanoparticles for detection and treatment of cancer. Adv Mater. 2012.

[11] Graham D, Goodacre R. Chemical and bioanalytical applications of surface enhanced Raman scattering spectroscopy. Chem Soc Rev. 2008;37:883–4.

[12] Zhang XG, Zhang XL, Luo CL, Liu ZQ, Chen YY, Dong SL, et al. Volume-enhanced Raman scattering detection of viruses. Small. 2019;1805516.

[13] Cheng ZQ, Li ZW, Xu JH, Yao R, Li ZL, Liang S, et al. Morphology-controlled fabrication of large-scale dendritic silver nanostructures for catalysis and SERS applications. Nanoscale Res Lett. 2019;14:89.

[14] Kolataj K, Krajczewski J, Kudelski A. Silver nanoparticles with many sharp apexes and edges as efficient nanoresonators for shell-isolated nanoparticle-enhanced Raman spectroscopy. J Phys Chem C. 2017;121:12383–91.

[15] He RX, Liang R, Peng P, Zhou YN. Effect of the size of silver nanoparticles on SERS signal enhancement. J Nanopart Res. 2017;19:267.

[16] Lee CH, Hankus ME, Tian LM, Pellegrino PM, Singamaneni S. Highly sensitive surface enhanced Raman scattering substrates based on filter paper loaded with plasmonic nanostructures. Anal Chem. 2011;83:8953–8.

[17] Eshkeiti A, Narakathu BB, Reddy ASG, Moorthi A, Atashbar MZ, Rebrosova E, et al. Detection of heavy metal compounds using a novel inkjet printed surface enhanced Raman spectroscopy (SERS) substrate. Sens Actuators B. 2012;171–2:705–11.

[18] Singh JP, Chu HY, Abell J, Tripp RA, Zhao YP. Flexible and mechanical strain resistant large area SERS active substrates. Nanoscale. 2012;4:3410–4.

[19] Aksu S, Huang M, Artar A, Yanik AA, Selvarasah S, Dokmeci MR, et al. Flexible plasmonics on unconventional and nonplanar substrates. Adv Mater. 2011;23:4422–30.
[20] Xu WG, Ling X, Xiao JQ, Dresselhaus MS, Kong J, Xu HX, et al. Surface enhanced Raman spectroscopy on a flat graphene surface. Proc Natl Acad Sci U S A. 2012;109:9281–6.
[21] Chen HJ, Wang YL, Dong SJ, Wang E. An approach for fabricating self-assembled monolayer of Ag nanoparticles on gold as the SERS-active substrate. Spectrochim Acta Part A. 2006;64:343–8.
[22] Polavarapu L, Liz-Marzan LM. Towards low-cost flexible substrates for nanoplasmonic sensing. Phys Chem Chem Phys. 2013;15:5288–300.
[23] Chen JM, Huang YJ, Kannan P, Zhang L, Lin ZY, Zhang JW, et al. Flexible and adhesive surface enhance Raman scattering active tape for rapid detection of pesticide residues in fruits and vegetables. Anal Chem. 2016;88:2149–55.
[24] Wang KQ, Sun DW, Pu HB, Wei QY, Huang LJ. A stable, flexible and high performance SERS chip enabled by a ternary film-packaged plasmonic nanoparticle array. ACS Appl Mater Interfaces. 2019;11(32):29177–86.
[25] Xu KC, Zhou R, Takei K, Hong MH. Toward flexible surface-enhanced Raman scattering (SERS) sensors for point-of-care diagnostics. Adv Sci. 2019;1900925.
[26] Lian XX, Sun HL, Lv YJ, Wang GX. Room temperature self-assembled Ag nanoparticles/Mo-37.5% Ag film as efficient flexible SERS substrate. Mater Lett. 2020;275:128164.
[27] Huang XX, Sun HL, Wang GX, Stock HR. Self-formation of Ag particles/Ag-Zr alloy films on flexible polyimide as SERS substrates. Appl Surf Sci. 2019;487:1341–57.
[28] Zada N, Khan I, Shah T, Gul T, Khan N, Saeed K. Ag-Co oxides nanoparticles supported on carbon nanotubes as an effective catalyst for the photodegradation of Congo red dye in aqueous medium. Inorg Nano-Met Chem. 2020;50.
[29] Zhang XH, Zhang Y, Tian BH, Song KX, Liu P, Jia YL, et al. Review of nano-phase effects in high strength and conductivity copper alloys. Nanotechnol Rev. 2019;8:383–95.
[30] Feng J, Song KX, Liang SH, Guo XH, Jiang YH. Electrical wear of TiB_2 particle-reinforced Cu and Cu–Cr composites prepared by vacuum arc melting. Vacuum. 2020;175:109295.
[31] Li SL, Guo XH, Zhang SL, Feng J, Song KX, Liang SH. Arc erosion behavior of TiB_2/Cu composites with single-scale and dual-scale TiB_2 particles. Nanotechnol Rev. 2019;8(1):619–27.
[32] Zhang XH, Zhang Y, Tian BH, Jia YL, Liu Y, Song KX, et al. Cr effects on the electrical contact properties of the Al_2O_3-Cu/15W composites. Nanotechnol Rev. 2019;8:128–35.
[33] Feng J, Liang SH, Guo XH, Zhang Y, Song KX. Electrical conductivity anisotropy of copper matrix composites reinforced with SiC whiskers. Nanotechnol Rev. 2019;8:285–92.
[34] Zhang XH, Zhang Y, Tian BH, Jia YL, Liu Y, Song KX, et al. Thermal deformation behavior of the Al_2O_3-Cu/(W, Cr) electrical contacts. Vacuum. 2019;164(6):361–6.
[35] Long F, Guo XH, Song KX, Jia SG. Enhanced arc erosion resistance of TiB_2/Cu composites reinforced with the carbon nanotube network structure. Mater Des. 2019;108136.
[36] Zhang XH, Zhang Y, Tian BH, An JC, Zhao Z, Volinsky AA, et al. Arc erosion behavior of the Al_2O_3-Cu/(W, Cr) electrical contacts. Composites Part B. 2019;160(3):110–8.
[37] Zhang XH, Zhang Y, Tian BH, Jia YL, Fu M, Liu Y. Graphene oxide effects on the properties of Al_2O_3-Cu/35W5Cr composite. J Mater Sci Technol. 2020;37(1):185–99.
[38] Sarakinos K, Greczynski G, Elofsson V, Magnfalt D, Hogberg H, Alling B. Theoretical and experimental study of metastable solid solutions and phase stability within the immiscible Ag-Mo binary system. J Appl Phys. 2016;119:095303.
[39] Ossai CI, Raghavan N. Nanostructure and nanomaterial characterization, growth mechanisms, and applications. Nanotechnol Rev. 2018;7(2):209–31.
[40] Gao T, Wang YQ, Wang K, Zhang XL, Dui JN, Li GM, et al. Controlled synthesis of homogeneous Ag nanosheet-assembled film for effective SERS substrate. ACS Appl Mater Interfaces. 2013;5:7308–14.
[41] Sun HL, Huang XX, He MJ, Lian XX, Wang GX. Preparation and controllability of Cu particles on annealed Mo-Cu alloy films. Mater Lett. 2019.
[42] Quan JM, Zhu Y, Zhang J, Li JY, Wang N. High-performance surface-enhanced Raman scattering substrate prepared by self-assembling of silver nanoparticles into the nanogaps of silver nanoislands. Appl Opt. 2017;56:5751–60.
[43] Kalwar K, Shen M. Electrospun cellulose acetate nanofibers and Au@AgNPs for antimicrobial activity – a mini review. Nanotechnol Rev. 2019;8:246–57.
[44] Tang J, Guo H, Zhao MM, Liu WY, Chou XJ, Zhang BZ, et al. Ag nanoparticles cladded with parylene for high-stability microfluidic surface-enhanced Raman scattering (SERS) biochemical sensing. Sens Actuators B. 2017.
[45] Zhang KB, Zeng TX, Tan XL, Wu WD, Tang YJ, Zhang HB. A facile surface-enhanced Raman scattering (SERS) detection of rhodamine 6G and crystal violet using Au nanoparticle substrates. Appl Surf Sci. 2015;347:569–73.
[46] Li XX, Lin X, Liu BK, Zhao XL, Zhao HY, Wang L, et al. Citrate-assisted galvanic replacement for fabrication of homogeneous Ag nanosheets as high performance SERS substrate. Appl Phys A. 2019;125:492.
[47] Zhang R, Xu BB, Liu XQ, Zhang YL, Xu Y, Chen QD, et al. Highly efficient SERS test strips. Chem Commun. 2012;48:5913–5.
[48] Wang YQ, Ma S, Yang QQ, Li XJ. Size-dependent SERS detection of R6G by silver nanoparticles immersion-plated on silicon nanoporous pillar array. Appl Surf Sci. 2012;258:5881–5.